Subcellular resolution 3D light field imaging with genetically encoded voltage indicators

Peter Quicke[a,b], **Carmel L. Howe**[a,b], **Pingfan Song**[c], **Herman Verinaz Jadan**[c], **Chenchen Song**[d], **Thomas Knöpfel**[d,b], **Mark Neil**[e,b], **Pier Luigi Dragotti**[c], **Simon R. Schultz**[a,b*], **Amanda J. Foust**[a,b**]

[a]Department of Bioengineering, Imperial College London, London, UK
[b]Centre for Neurotechnology, Imperial College London, London, UK
[c]Department of Electrical and Electronic Engineering, Imperial College London, London, UK
[d]Department of Brain Sciences, Imperial College London, London, UK
[e]Department of Physics, Imperial College London, London, UK

Abstract. Light field microscopy (LFM) enables high signal-to-noise ratio (SNR), light efficient volume imaging at fast frame rates, and has been successfully applied to single-cell resolution functional neuronal calcium imaging. Voltage imaging with genetically encoded voltage indicators (GEVIs) stands to particularly benefit from light field microscopy's volumetric imaging capability due to high required sampling rates, and limited probe brightness and functional sensitivity. Previous LFM studies have imaged GEVIs to track population-level interactions only in invertebrate preparations and without single cell resolution. Here we demonstrate sub-cellular resolution GEVI light field imaging in acute mouse brain slices resolving dendritic voltage signals localized in three dimensions. We characterize the effects of different light field reconstruction techniques on the SNR and signal localization and compare the SNR to fluorescence transients imaged in wide field. Our results demonstrate the potential of light field voltage imaging for studying dendritic integration and action potential propagation and backpropagation in 3 spatial dimensions.

Keywords: light field microscopy, genetically encoded voltage indicator, voltage imaging.

*Simon R. Schultz, s.schultz@ic.ac.uk **Amanda J. Foust, a.foust@ic.ac.uk

1 Introduction

Cellular resolution voltage imaging enables direct observation of neuronal computation. Indeed, membrane potential imaging experiments have spatiotemporally resolved both active and passive action and synaptic potential generation throughout dendritic and axonal arbors.[1-14] Resolution of these small voltage signals at high speeds requires high photon fluxes, making wide field single photon (1P) imaging by far the most common voltage imaging modality. Imaging neuronal processes with this technique requires the imaged membranes to lie approximately flat in the microscope's focal plane. As these experiments are typically performed in slices, the requirement for flat, healthy, and superficial cells represents a significant barrier to entry for experimenters.

10 Even in the best-prepared slices, anatomy dictates that only a few cells will be oriented parallel to

11 the surface, reducing experimental throughput, and only certain cell types feature morphology that

12 can be well-sampled by a single plane. Multiple approaches to improving wide field imaging's

13 3D performance have been developed. Anselmi *et al.* (2011)[15] applied remote focusing to axially

14 shift and tilt the wide field focal plane as required by the sample, enabling calcium imaging along

15 tilted dendrites. This adaptation, however, costs half of the fluorescence emission and is limited to

16 a single tilted plane at a time. Point spread function (PSF) engineering via cubic phase masks[16] or

17 spherical aberration[17] also enables parallelised volumetric sample imaging when combined with

18 light sheet excitation, however to our knowledge these approaches have not successfully been im-

19 plemented to image membrane voltage.

20   Lack of optical sectioning with wide field 1P imaging further complicates matters. Light from

21 out-of-focus structures pollutes in-focus signals, confounding allocation of signals to axially sep-

22 arated processes. This issue is difficult to resolve with traditional optically sectioning confocal

23 or two-photon microscopy approaches as they are point scanning. Sequential sampling of each

24 pixel greatly reduces imaging bandwidth, and the fast frame rates required for voltage imaging

25 necessitates short dwell times and therefore few collected photons. This restricts Poisson-noise

26 limited SNR to low levels, making point scanning voltage imaging applicable to a limited number

27 of experimental paradigms.[12,18–20]

28   Fluorescence excitation parallelization into multiple spots,[21–27] blobs,[28,29] lines,[30–32] sheets,[33–40]

29 or specified patterns[41–45] increases the photon budget, enabling functional volumetric imaging or

30 single-plane imaging at increased speeds. A small number of these have been applied to imaging

31 voltage in 2 dimensions,[26,31,42,45] however they are not able to image neuronal processes in 3D.

32 Many of these techniques also trade-off reduced robustness to scattering compared to single-point

33   scanning modalities for the increased excitation from parallelization.

34   Parallelized 3D two-photon imaging with elongated Bessel[46,47] or stereoscopic tilted[48] beams

35   excites narrow columns of fluorescence and relies on temporal and spatial sparsity of labelling and

36   activity to demix time courses from different z planes. This increases the volume rate but each

37   columnar pixel is still addressed sequentially, limiting bandwidth. These techniques have been

38   used to image calcium fluorescence transients but not yet voltage.

39   Light field microscope (LFM)[49] enables reconstruction of 3D volumes from single 2D camera

40   images, extending wide field imaging whilst maintaining its unparalleled fluorescence excitation

41   and collection efficiency. This is achieved by inserting a microlens array (MLA) at the native

42   image plane of the microscope and placing the image sensor at its back focal plane (Fig. 1a).

43   This disperses the angular components of the collected image (Fig. 1b), which can be used to

44   infer objects' axial positions. Each LFM image consists of circular subimages (Fig. 1c), with

45   each subimage resembling a pixel in an undersampled image of the scene. Within each circular

46   subimage, each pixel location encodes a different angular sampling through the object intersecting

47   with the subimage's location, a columnar tomographic projection through the sample.[50] Light field

48   images are typically parameterized by the 4D function $\mathcal{L}(u, v, x, y)$, where each lenslet subimage

49   is $\mathcal{L}(u, v, \cdot, \cdot)$ and the same specific pixel under each subimage is $\mathcal{L}(\cdot, \cdot, x, y)$. The 'native LFM

50   resolution' with which the object is laterally sampled is given by the microlens pitch divided by

51   the objective magnification, much worse than the corresponding wide field resolution. In exchange

52   the microlenses provide angular information that can be used to render views of the object from

53   different perspectives, focus on different planes, and reconstruct 3D volumes all from a single 2D

54   frame. This technique converts a key disadvantage of wide field 1P fluorescence excitation, lack

55   of optical sectioning, into an advantage, as out-of-focus light renders 3D information about the

56   sample.

57   Two prominent algorithms for reconstructing source volumes from LFM images have been described, synthetic refocusing[49] and 3D deconvolution.[50] Synthetic refocusing relies on a ray optics model of LFM image formation to reconstruct images at the native LFM resolution equivalent to those of a wide field microscope focused at any axial plane in the sample. Focal stacks can be generated similar to standard microscope z-stacks by combining images reconstructed at multiple axial depths. Each pixel in the refocused image is a weighted sum of light field image pixels, meaning refocusing is fast. The reconstructed images, however, suffer from the same blur due to lack of optical sectioning as a standard wide field microscope.

65   An alternative approach is based on reconstruction of the source volume using a forward model of light-field image formation (the LFM PSF) based on wave optics.[50] Iterative deconvolution approaches such as Richardson-Lucy (RL)[51,52] or the Image Space Reconstruction Algorithm (ISRA)[53] find the maximum likelihood source volume given the measured image and LFM PSF in the presence of Poissonian (RL) or Gaussian (ISRA) noise. This approach is able to reconstruct source volumes at a lateral resolution greater than the native LFM resolution (the MLA pitch in the sample) by leveraging the fine sampling of the LFM tomographic projections.[50] This increased resolution reconstruction fails where the tomographic sampling is degenerate, most notably around the native focal plane of the microscope, although newer designs have circumvented this limitation.[54–57] The source volume is also reconstructed with less axial blur than in the refocused case, increasing axial signal discriminability.

76   Electrical length constants in neurons are on the scale of tens to hundreds of microns, making increased lateral pixel size less disadvantageous for voltage imaging. Over-resolving electrical fluctuations by imaging at or below the diffraction limit is typically unnecessary and can even hurt

4

79 SNR by increasing the relative impact of non-Poisson noise such as read noise. Spatial resolu-

80 tion is therefore often sacrificed in voltage imaging experiments to increase speed or SNR. Many

81 such experiments use low read noise, high sensitivity CCD sensors featuring low pixel counts,

82 with pixels often measuring several microns across in the sample plane. Even with higher pixel

83 count detectors, the relatively low sensitivity of many voltage probes means multiple pixels are

84 often binned to increase SNR to acceptable levels. LFM's decreased native lateral sampling rate

85 therefore suits voltage imaging well, and deconvolution of LFM voltage imaging time series can

86 be implemented without oversampling to reduce computational cost.

87 LFM has successfully imaged calcium over large volumes in C. elegans and zebrafish,[58,59] and

88 in both head-fixed and behaving mice.[60–62] Voltage dynamics have also been imaged successfully

89 without single-cell resolution in Drosophila[63] and larval zebrafish[64] as part of whole brain imaging

90 setups alongside calcium imaging. LFM has not, to our knowledge, been applied to studying sub-

91 cellular or single-cell resolution voltage dynamics in any sample, despite its apparent suitability. In

92 this study we apply LFM to sub-cellular GEVI imaging in acute mouse brain slices. We combine

93 this technique with a recently reported transgenic strategy driving sparse expression in a random

94 subset of layer 2/3 cortical pyramidal neurons which enables the resolution of single-cell level

95 voltage signals in neuronal somata and dendrites.[65,66]

96 We demonstrate that LFM is able to simultaneously image axially separated dendrites, enabling

97 single-shot capture and localisation of GEVI fluorescence transients in the 3D dendritic arbour.

98 We compare and evaluate deconvolution and synthetic refocusing for different GEVI imaging ap-

99 plications, whilst using a coarse deconvolution approach with no lateral oversampling to reduce

100 computational cost. We also apply a recently developed LFM PSF calculation[67] for high NA ob-

101 jectives. We show that LFM enables 3D localization of dendritic and somatic GEVI fluorescence
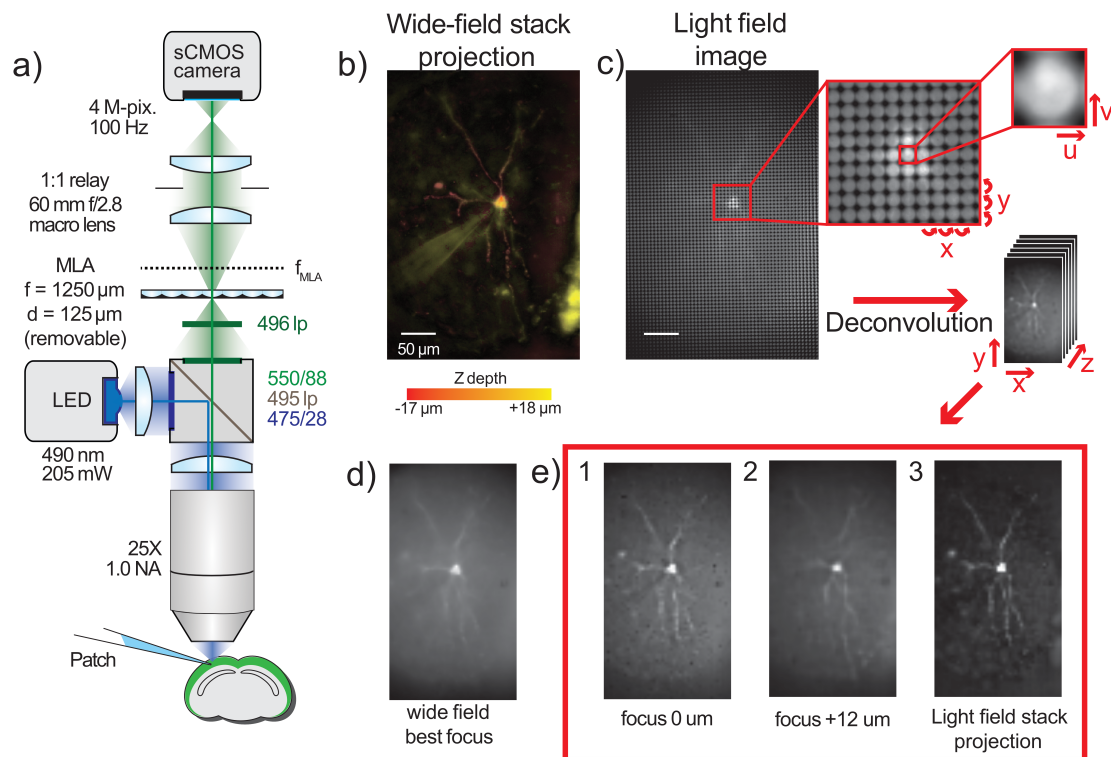
5

Fig 1 Light field microscopy enables simultaneous focusing on axially separated dendrites. a) LFM Diagram b) A pseudocolour z-projection of a wide field image stack through a GEVI labelled cell. Depth is color coded from red (superficial) to yellow (deep). Individual dendrites follow tortuous paths in all 3 dimensions, making simultaneous focussing on them all impossible in wide field microscopy. c) A light field image of the same cell showing the structure of light field images. Each spot in the light field image is a spatial sampling (coordinates x,y) of the angular distribution of rays (coordinates u,v) at that point. This angular and spatial information can be used to reconstruct a volume from a single image. d) A best focus wide field image of the single cell showing partially in focus dendritic structures. e) Three different images recovered from the light field image: 1 & 2) Single axial planes deconvolved showing individual dendrites seen out of focus in the wide field image. 3) A z-projection through the recovered light field volume image showing the in-focus sections of recovered dendrites. Figure adapted from Quicke (2019)[68] CC BY-SA 4.0.

102 transients and compare the extent to which refocused and deconvolved light fields enable lateral

103 and axial transient localization. Finally, we compare temporal signal SNR between LFM and wide

104 field microscopy.

6

105 2 Methods

106 This section reproduces methods described in Quicke (2019).[68] We designed our LFM following

107 the principles set out by Levoy *et al.* (2006).[49] We adapted a wide field imaging system by placing

108 a microlens array (MLA) at the microscope image plane, and used a 1:1 relay lens (Nikon 60 mm

109 f/2.8 D AF Micro Nikkor Lens) system to image the MLA back focal plane onto our camera chip

110 (ORCA Flash 4 V2, 2048×2048 pixels, $6.5\,\mu m$ pixel size, Hamamatsu, see Figure 1a.). The lateral

111 resolution is given by the MLA pitch divided by the magnification of the objective. Using our $25\times$

112 objective (1.0 NA, XLPLN25XSVMP, Olympus) we chose our system to have $5\,\mu m$ lateral pixels,

113 dictating a microlens pitch of $125\,\mu m$.

114 The axial resolution is defined by the number of resolvable diffraction-limited spots behind

115 each microlens.[49] Assuming a central emission wavelength of 550 nm for mCitrine, the FRET

116 donor in VSFP-Butterfly 1.2,[69] the spot size in the camera plane is $6.46\,\mu m$ using the Sparrow

117 criterion. With an $125\,\mu m$ pitch MLA, we are able to resolve $N_u = 19$ distinct spots under each

118 microlens. The depth of field when synthetically refocussing our LFM can therefore be calculated

119 as $7.81\,\mu m$.[49]

120 To efficiently use the camera sensor, the exit pupil of the objective should map through the

121 MLA to produce circles on the light field plane that are just touching, requiring that the objective

122 image-side f-number (f/12.5) equal the MLA f-number. We chose an f/10 MLA (MLA-S125-f10,

123 RPC Photonics), an off-the-shelf part which came close to matching whilst being a larger aperture.

124 *2.1 Imaging*

125 This study was carried out in accordance with the recommendations of UK Animals (Scientific

126 Procedures) Act 1986 under Home Office Project and Personal Licenses (project licenses 70/7818

7

127 and 70/9095). Slices were made from 4 mice aged 31, 32, 32 and 175 days transgenically mod-

128 ified to sparsely express VSFP Butterfly 1.2[69] using the method previously described in Song *et*

129 *al.* (2017).[65,66] These transgenic mice express the GEVI in cortical layer 2/3 pyramidal neurons

130 under the intersectional control of TetO and destabilised Cre-recombinase.[70–72] The destabilised

131 Cre-recombinase was stochastically re-stabilised to induce sparse expression of the voltage indi-

132 cator via two IP injections of a total of $2 \times 10^{-4}\,\mathrm{mg\,kg^{-1}}$ Trimethoprim (TMP, Sigma) over 2

133 consecutive days as described in Song *et al.* (2017).[66]

134   Slices were prepared at least 2 weeks post TMP injection using a method adapted from Ting et

135 al. (2014)[73] (the 'protective recovery' method, www.brainslicemethods.com). $400\,\mu\mathrm{m}$ slices were

136 cut with a Camden Microtome 7000 in ice cold 95% O_2 / 5% CO_2 oxygenated ACSF containing:

137 (in mM) 125 NaCl, 25 $NaHCO_3$, 20 glucose 2.5 KCl, 1.25 NaH_2PO_4, 2 $MgCl_2$, 2 $CaCl_2$. The

138 slices were then immediately transferred into NMDG-ACSF[73] containing: (in mM) 110 N-methyl-

139 D-Glucamine, 2.5 KCl, 1.2 NaH_2PO_4, 25 $NaHCO_3$, 25 Glucose, 10 $MgCl_2$, 0.5 $CaCl_2$, adjusted

140 to 300-310 mOsm/Kg, pH 7.3-7.4 with HCl and oxygenated with 95% O_2 / 5% CO_2 at $36\,°\mathrm{C}$ for

141 12 minutes before being transferred back into the original sodium-containing ACSF for at least an

142 hour before patching and imaging.

143   Fluorescent cells were patched under oblique infrared illumination (780 nm) with pipettes of

144 resistances between 3 and 10 MOhms when filled with intracellular solution containing: (in mM)

145 130 K-Gluconate, 7 KCl, 4 ATP - Mg, 0.3 GTP - Na, 10 Phosphocreatine - Na, 10 HEPES. We

146 digitized current clamp signals (Power 1401 digitizer; Cambridge Electronic Design) from a Multi-

147 clamp 700B amplifier (Axon Instruments). At room temperature, we imaged at 100 frames/second

148 for 2.5 seconds whilst injecting current pulses lasting 50 and 100 ms. Each pulse elicited depolar-

149 ization to threshold evoking a single action potential or burst of 2-3 action potentials. We powered

8

150 a 490 nm LED (M490L4, Thorlabs) with a constant current source (Keithley Sourcemeter 1401) to

151 illuminate the sample at 3-11 mW/mm^2. Sets of light field and wide field time series acquisitions

152 were interleaved by removing and replacing the microlens array by hand. We averaged between 4

153 and 16 sweeps per imaging condition. The LED was collimated with an f = 16 mm aspheric lens

154 (ACL25416U0-A, Thorlabs) and filtered with a 475/28 nm excitation filter (FITC-EX01-CLIN-25,

155 Semrock). Fluorescence was collected using a 495 nm long pass dichroic (FF495-Di03, Semrock)

156 along with a 550/88 nm collection filter (FF01-550/88, Semrock) and 496 long pass filter (Sem-

157 rock FF01-496/LP) to attenuate any excitation light transmitted by the dichroic. Imaging data were

158 acquired with Micromanager.[74] Imaged cells' somata lay between 11 and $40\,\mu m$ below the slice

159 surface, with a median depth of $29\,\mu m$. Data were analysed with custom Python scripts using SciPy

160 packages.[75]

161 *2.2 Light field reconstruction*

162 We reconstructed source volumes using two techniques to compare their performance for single-

163 cell voltage data. We calculated (x,y,z,t) volume time series using synthetic refocussing,[49] and

164 ISRA[53,58] using a PSF calculated using the method described in the section below. RL decon-

165 volution[50–52] was also tested on the data, however little discernible difference in the results was

166 observed.

167 *2.2.1 Light field PSF calculation*

168 We calculated LFM PSFs differently to previously described,[50] using the method described in

169 Quicke *et al.* (2019).[67,68] Briefly, to calculate the field at the microlens array we considered how

170 a high NA objective lens collects the field from an oscillating electric dipole at position **r** near

9

171 the microscope focus, $|\mathbf{r}| \ll f$, at the origin, calculating the Fourier transform of the field in

172 the objective back focal plane. We assumed that we could model the behaviour of a point source

173 consisting of randomly oriented fluorescent molecules as the incoherent sum of dipoles along 3

174 orthogonal directions. We then used the same method as described in Broxton *et al.* (2013)[50] to

175 model transmission through the MLA and to the camera.

176   We calculated the PSF for GEVI imaging deconvolution for 550 nm emission. We did not

177 oversample the deconvolution as resolving voltage signals generally requires averaging pixels to

178 approximately the native LFM resolution. We therefore generated a single light field kernel for

179 each depth by averaging over kernels sampled for point sources at different lateral positions under

180 the microlens, weighting each point in the average by a 2D Hamming window function of a width

181 equal to our microlens' pitch. We averaged over kernels sampled at 5 times finer than the native

182 microlens resolution. The ISRA was used to deconvolve the data.

183 *2.2.2 Volume reconstructions*

184 Having obtained our downsampled PSF we deconvolved our volume using a similar procedure to

185 previous studies. A key difference is that only a single 2D convolution was required for each depth

186 in the reconstructed volume for the forwards and backwards projections, respectively, as we did

187 not increase the lateral sampling rate. We applied the deconvolution scheme independently to each

188 frame of the image time sequences, using a cluster to parallelize the data processing. Deconvolu-

189 tion of a single frame took around 30 - 40 minutes for a 21 iteration deconvolution of 21 z-planes

190 on a single CPU. We employed a large cluster to process the individual frames simultaneously,

191 enabling 5000 frames to be processed overnight. We did not use a parallel algorithm within each

192 deconvolution to leverage, e.g., GPU processing, as the computing resources available to us were

10

193 better suited to data parallelism. As with previous studies this would greatly increase the rate of

194 individual frames, although it would also likely reduce the number of simultaneous frames that

195 could be deconvolved for typical cluster setups.

196   Synthetic refocusing, based on a ray optics model of light field image formation, is a simpler

197 approach to volume reconstruction that is also much less computationally intensive. Images fo-

198 cused at different z-depths can be constructed by combining individual perspective views using the

199 formula derived in Ng *et al.* (2005).[76] Linear interpolation in this summation results in each pixel

200 being the weighted sum of pixels of the original light field image. This reconstruction is much

201 faster than the iterative deconvolution methods and also does not suffer from noise amplification.[77]

202 *2.3 Volume time series analysis*

203 *2.3.1 Effect of reconstruction on SNR*

204 To compare the effect of different reconstruction techniques on voltage signal SNR we recon-

205 structed single planes from volumes at the light field microscope focus. We compared synthetically

206 refocused time series with time series deconvolved using ISRA for different iteration numbers. Re-

207 gions of interest (ROIs) were manually chosen over the soma and its surround and were identical

208 for the synthetically refocused and deconvolved volumes.

209   As we were collecting fluorescence from the VSFP Butterfly 1.2 FRET donor, fluorescence

210 decreased upon membrane depolarisation.[69] Therefore the traces shown Figures 2 and 3 are in-

211 verted. To measure SNR we calculated the signal as the 5th percentile value during a stimulus and

212 relaxation period of 200 ms with the median value of the 100 ms before the stimulation period

213 subtracted. The noise level was calculated as the standard deviation of a 350 ms period during no

214 intracellular current stimulus.

11

2.3.2 Depth-time plots

216   To determine the center of mass of the signal for different cellular ROIs we extracted time courses

217   from each refocused or deconvolved depth, then filtered the resulting depth-time 2D arrays with a

218   median filter of 11 samples in the time axis (110 ms) and 3 samples in the z axis ($15\,\mu m$).

2.3.3 Comparison of light field and wide field SNR

220   We compared the SNR between trials of the same cell for image sequences taken with wide field

221   and light field imaging systems. We compared the SNR between refocused and wide field images

222   for the same number of repeats using ROIs calculated to be the same for both imaging modalities.

223   For 8/12 cells, an extra aperture was introduced into our light field microscope to compensate

224   for chromatic aberration, reducing the light throughput of the microscope by between 1/2 and 3/4

225   during light field imaging compared to the equivalent wide field trials. To account for this, the SNR

226   for these trials was adjusted by a factor equal to the square root of the ratio of the mean brightness

227   of the first imaging trials from the light field and wide field trials. The microscope was realigned

228   to account for chromatic aberration before the final 4/12 cells, meaning the design light throughput

229   of the microscope was the same between light field and wide field trials. For these trials the raw

230   SNR was included in the analysis.

2.3.4 Signal spread analysis

232   We compared the lateral and axial signal spread using a method similar to our previous work.[65] We

233   quantified the neuronal voltage signal strength in each pixel to create 2- or 3-D 'activation maps'

234   by calculating the temporal correlation coefficient of each pixel's time course with a seed time

235   course from the somatic ROI.

236 We compared the spatial autocorrelations of these activation maps to quantify the average sig-

237 nal crosstalk between cellular voltage signals.[65] In our previous work we described how the auto-

238 correlation can be used to quantify the average signal power a cell contributes to a specific pixel's

239 time course and quantified this effect for this preparation with wide field microscopy in 2 dimen-

240 sions.[65] In this work, we calculated the 3D autocorrelations of the lightfield volumes and 2D

241 autocorrelations of the wide field volumes using Fast Fourier Transform based convolution, setting

242 the central 10×10 pixels of the autocorrelations to the mean of their perimeter to remove a central

243 noise peak.

3 Results

244

3.1 Light Field Microscopy Enables Simultaneous Imaging of Axially Separated Dendrites.

245

246 We demonstrated LFM's ability to resolve axially separated structures by imaging a cell with a

247 complex 3D dendritic arbour using both wide field and light field microscopy (Fig. 1b) and LFM

248 (Fig. 1c). No single plane wide field image was able to simultaneously bring all the dendrites into

249 a good focus (Fig. 1d), however in different planes from a volume reconstructed by deconvolution

250 different dendritic structures could be clearly distinguished (Fig. 1e1 & Fig. 1e2). The same

251 cellular features can clearly be seen in a standard deviation projection through the reconstructed

252 LFM stack (Fig. 1e3) and a wide field z stack through the same cell (Fig. 1b, both projections

253 through stacks at $1\,\mu\text{m}$ axial increments).

3.2 Comparison of the Effect of Different Reconstruction Methods on Signal-to-Noise Ratio

254

255 Low-sensitivity GEVIs mean SNR is of utmost importance in voltage imaging analysis strategies,

256 and so we first compared the performance of the deconvolution and refocusing reconstruction ap-
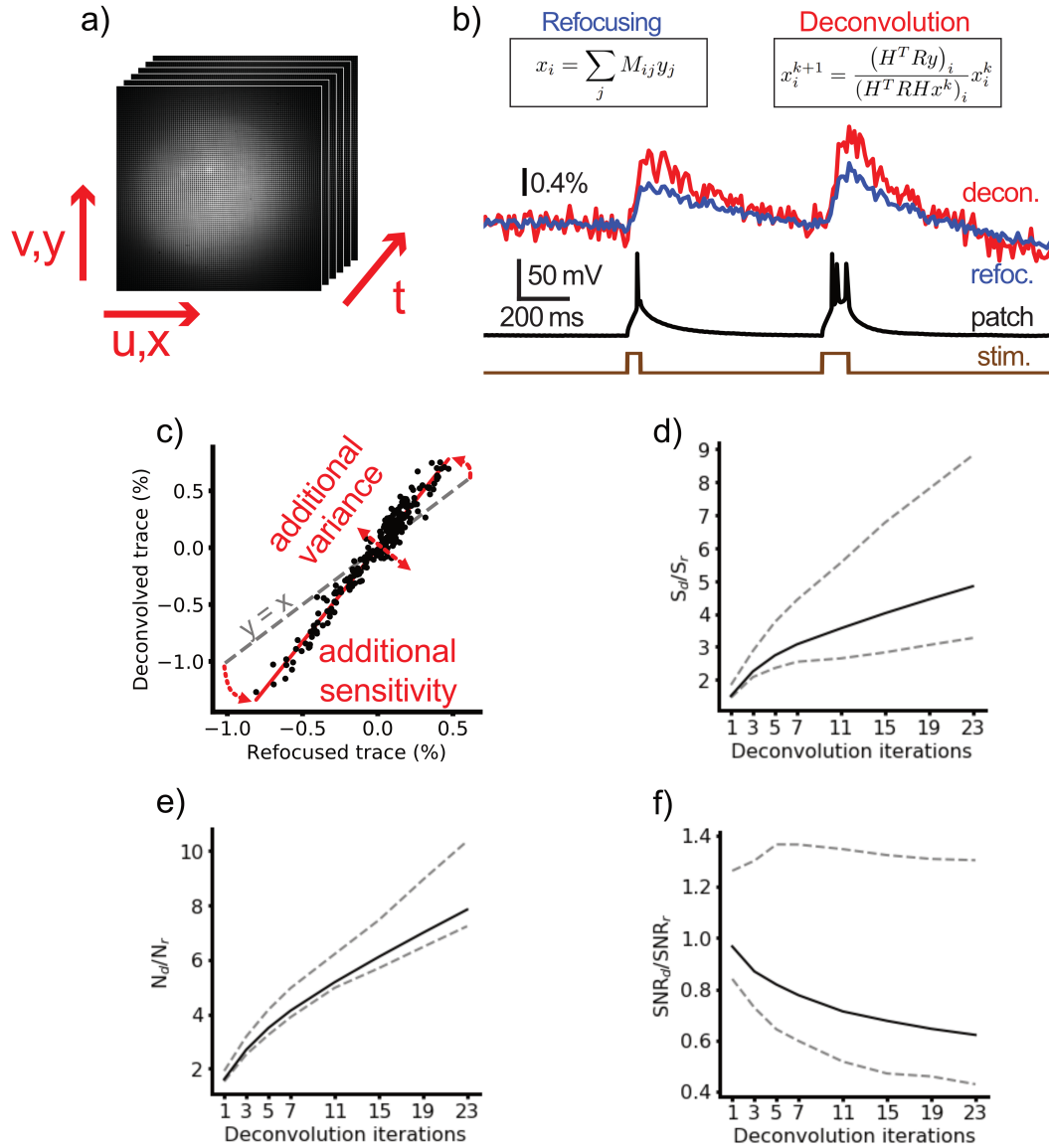
Fig 2 Comparison of different reconstruction methods on SNR. a) Light field time series were collected of functional voltage signals from sparsely expressed GEVIs. b) Time series were extracted from in focus image sequences of the soma via refocusing (left) and ISRA deconvolution (right) and the signal and noise were compared. c) Deconvolved and refocused signals are strongly linearly correlated, as can be seen from plotting the individual trace time points. The additional noise variance due to deconvolution can be identified as the residual from the linear fit. The increased signal level can be seen as the increased fit gradient over unit slope (grey dashed line). Both the noise d) and the signal e) increase monotonically with increasing deconvolution iteration, leading to an overall reduction in SNR with iteration number f). At low iteration number the deconvolution and refocusing are very similar. At large iteration number the SNR is decreased relative to refocused; however, increased axial sectioning may still motivate the use of deconvolution methods. Solid lines are median of n = 15 cells, dashed lines indicate 25th and 75th percentile values. Traces in b) were generated from an average of 8 sweeps.

14

257 proaches on this metric. We reconstructed volume time series for 15 cells from LF time series (Fig

258 2a) and extracted optical time courses from ROIs over the individual cell's soma at the native focal

259 plane and compared the SNR between deconvolved and refocused volumes (Fig. 2b). Commonly

260 used LFM iterative reconstruction schemes are prone to noise amplification[78] which increases with

261 iteration number. It is therefore crucial to understand when to stop the iteration scheme. We used

262 the refocused images as a baseline comparison for the iteration analysis due to the ease of their

263 reconstruction. We found that for all iteration numbers the noise and signal level was increased

264 by deconvolution which increased sensitivity and variance (Figs. 2c - e). The signal significantly

265 increased from 0.3 (0.2, 0.4) % (all results presented as median (IQR)) in the refocused time series

266 to 1.4 (0.9, 1.7) % for the 21 iteration deconvolved traces (Wilcoxon signed rank, $n = 15$, $z = 0.0$,

267 $p = 0.0003$). The noise significantly increased from 0.05 (0.04, 0.08) % in the refocused time

268 series to 0.4 (0.3, 0.5) % for the 21 iteration deconvolved traces (Wilcoxon signed rank, $n = 15$,

269 $z = 0.0$, $p = 0.0002$). This resulted in the SNR reducing from approximately the same as the refo-

270 cused (1.0 (0.8,1.3)) case for a single deconvolution iteration to around half that of the refocused

271 case (0.6, (0.4, 1.3)). We also processed the light field time series using RL deconvolution and

272 found no substantial differences compared to ISRA.

273 *3.3 Light Field Microscopy Resolves 3D Localised and Axially Separated Voltage Signals*

274 We then explored a key advantage of sub-cellular resolution light field voltage imaging: 3D imag-

275 ing of neuronal processes. Achieving this requires signals from different planes to be discriminable

276 in volume reconstructions. Axial discriminability depends on intrinsic factors such as depth of

277 field, and also extrinsic factors, such as cellular morphology and signal spread due to tissue scat-

278 tering. To demonstrate the resolution of subcellular voltage transients in 3D, we reconstructed 4D
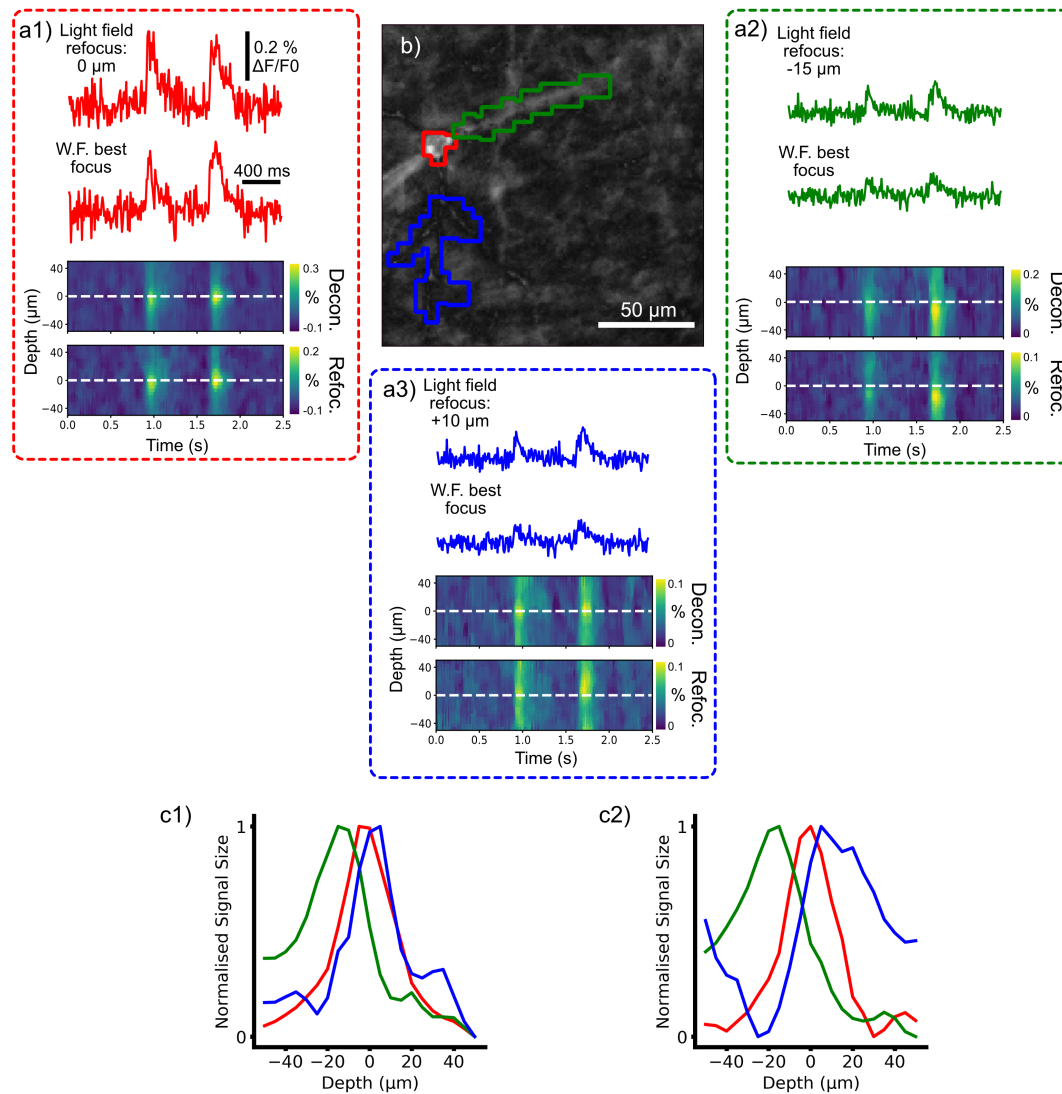
15

Fig 3 Deconvolution Light field microscopy resolves 3D localised voltage signals. a1-3) Time courses and depth-time plots showing signals from different cellular compartments (shown in (b)) localised at different depths. The somatic signal (a1) is maximal in the wide field and native light field focal planes, whilst the apical dendrite (a2) descends into the slice with its ROI localised 15 um deeper. The signal from a basal dendrite (a3) is superficial to the soma, and its best focal depth is difficult to localize due to the broad axial extent of the refocused signal. The basal and apical dendritic fluorescence transients in the wide field time courses have smaller signals than the light field signals as they are out of plane when focused on the soma. c) The normalised signal size for each ROI across different deconvolved (c1) and refocused (c2) depths. Deconvolution increases the axial localisation of signals. The data are an average of 8 sweeps.

16

279 (x,y,z,t) volumes from light field image time series and compared the temporal signals from ROIs

280 over different dendritic and somatic structures in multiple axial planes.

281   Figure 3 demonstrates LF imaging's ability to axially localize functional voltage signals from

282 neuronal processes and thereby image functional activity in 3D with SNR unachievable by any

283 equivalent wide field system. Panels 3a 1- 3) show single plane and multi-plane time courses from

284 three different ROIs over cellular compartments from a neuron distributed over multiple axial

285 planes. A somatic ROI (Fig. 3a1) in the native focal plane of both wide field and light field images

286 contains action potential evoked fluorescence transients approximately equal in signal size for both

287 light field and wide field (top). The depth-time plots show the functional signal localised to the

288 native focal plane in the LF functional stacks (bottom). In contrast, an ROI over the apical dendrite

289 (Fig. 3(1) has the largest signal when the LF image is refocused $15\,\mu m$ deeper into the slice, and

290 the signal in the equivalent wide field ROI is much smaller. The depth-time plots for this ROI from

291 both deconvolved and refocused stacks also clearly show the center of mass of the signal located

292 deeper than the native focal plane (Fig. 3(1), bottom). Signals from a basal dendrite (Fig. 3(3)

293 are similarly larger in the LF image refocused $10\,\mu m$ shallower than the native focal plane. The

294 corresponding depth-time plots show a slight shift in the signal center of mass to a shallower depth,

295 especially in the refocused case.

296   Plots of signal size as a function of depth for the refocused and deconvolved cases (Fig. 3c 1 &

297 2) show the axial localization as distinctly different planes for each ROI and also demonstrate a key

298 advantage of deconvolved over refocused reconstructions: increased accuracy in axial localization
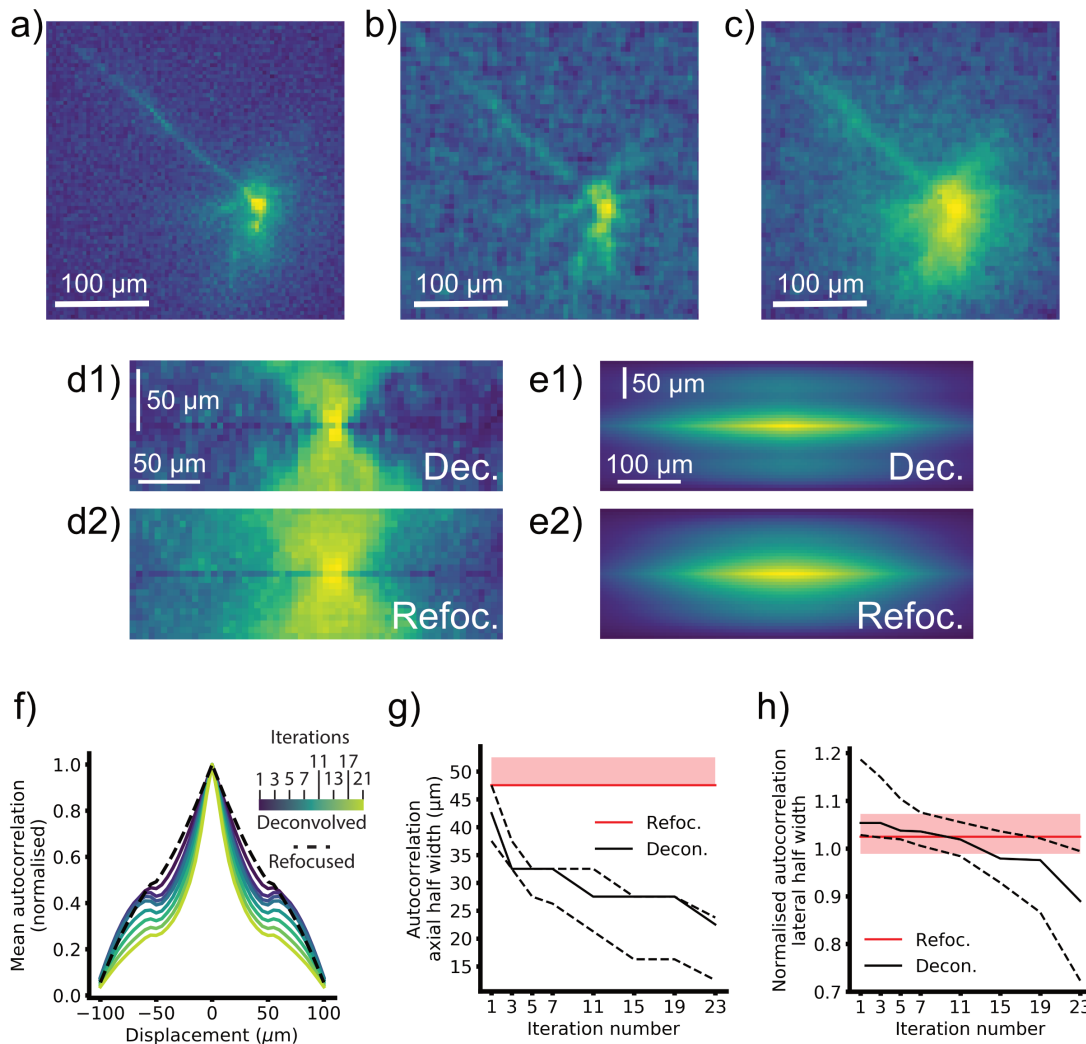
299 of functional signals.

17

Fig 4 Mapping dendritic signals. a) wide field activation image. b) Deconvolved activation image, sum projection from -35 to +35 um, 5 deconvolution iterations. c) Refocused activation image, sum projection from -35 to +35 um. d) x-z maximum intensity projections through deconvolved (top), and refocused (bottom) activation images showing the different axial sectioning. e) Mean x-z projections through the autocorrelations. f) Normalised maximum autocorrelation for different depths from refocused and deconvolved LFM activation volumes. The secondary peaks arise from the elongated axial PSF, and these can be seen decreasing as the iteration number increases. g) Median autocorrelation axial half widths for n = 12 cells with iteration number. Dashed lines represent quartile values. Red line is the refocused median width and shaded area the refocused interquartile range (IQR). h) Median autocorrelation lateral widths normalised to wide field lateral widths for refocused images (red, shaded area IQR) and different deconvolution iterations (black lines, dashed lines IQR).

300 *3.4 Deconvolution Increases Axial Localisation of Functional Voltage Signals*

301 The transients from refocused volumes exhibit a larger axial PSF width compared to the decon-

302 volved traces (Fig. 3c). Hence these signals are smeared out, reducing distinguishability of signal

303 contributions from different planes. To quantify this effect we generated volumes showing the

304 distribution of functional signal. We generated a time course from an in focus somatic ROI and

305 calculated the temporal correlation coefficient of every pixel in the volume for refocused and de-

306 convolved volume time series. Pixels with high correlation coefficients are interpreted as having a

307 large response to the intracellular current injection, and so a volume map of these reveals morphol-

308 ogy of structures through which the functional signal propagates. Activation maps from wide field

309 imaging trials show blurring around the soma from out of focus basal dendrites (Fig. 4a). Com-

310 paratively, z-projections from a $70\,\mu m$ region around the soma generated from the deconvolved

311 activation volume (Fig. 4b) reveals the structures that cause this blur. A projection through $70\,\mu m$

312 around the focus from the refocused case shows significantly more blurring due to the poor axial

313 sectioning of this technique (Fig. 4c). We used the 3D autocorrelation of these activation maps to

314 quantify the spread of the signal in 3D (see section 2.3.4). We quantified how the peak autocorre-

315 lation from each cell, and therefore functional signal contribution, decayed axially. Axial smearing

316 can be seen in reconstructions from both deconvolution and refocusing (Fig. 4d), although the ef-

317 fect is much more severe in refocused traces. The smearing appears in the axial autocorrelation as

318 both broadening of the central peak and increased side lobes (Fig. 4e). The central peak width and

319 side lobes decrease with increased deconvolution iteration number (Fig. 4f & g), thus increasing

320 the axial sectioning.

321   The autocorrelation widths decreased significantly from 1 to 21 iterations (median dropped

19

322 from 42.5 (37.5, 47.5) µm to 22.5 (12.5, 23.75) µm, $z = 0$, $p = 0.002$), and for both cases the

323 axial spread was significantly lower than refocused (median of 47.5 (47.5, 52.5) µm, $p = 0.001$,

324 $p = 0.002$ for 1 and 21 iterations respectively). Significance tests were performed with a Friedman

325 χ^2 with post hoc Bonferroni-corrected Wilcoxon signed-rank tests (significant at $p < 0.017$). n =

326 12 cells from 12 slices from 4 mice. Friedman $\chi^2 = 24$, $p = 6 \times 10^{-6}$.

327   Finally we compared how deconvolution and refocusing affected lateral signal localization

328 compared to the equivalent wide field time series (Fig. 4h). We measured the width of radially av-

329 eraged autocorrelations normalised to matched wide field trials for the refocused and deconvolved

330 cases. We found that the lateral signal spread significantly decreased from 1 to 21 iterations (me-

331 dian dropped from 1.05 (1.03, 1.18) times larger than wide field trials to 0.89 (0.73, 0.99) times

332 larger, $Z = 0$, $p = 0.002$), from significantly larger than the WF and refocused at 1 iteration

333 ($z = 1$, $p = 0.003$ and $z = 0$, $p = 0.002$ respectively), to significantly smaller than the refocused

334 at 21 iterations ($z = 0.0$, $p = 0.003$). The refocused widths did not differ significantly from the

335 matched wide field trials (median 1.02 (0.99, 1.07) times larger, $z = 17$, $p = 0.08$). Significance

336 tests were performed with a Friedman χ^2 with post hoc Bonferroni-corrected Wilcoxon signed-

337 rank tests on the raw widths (significant at $p < 0.0083$). $n = 12$ cells from 12 slices from 4 mice.

338 Friedman $\chi^2 = 26$, $p = 9 \times 10^{-6}$.

339   In total our analyses reveal that deconvolution improves both axial and lateral signal local-

340 ization, but decreases temporal signal SNR compared to synthetic refocussing, with both effects

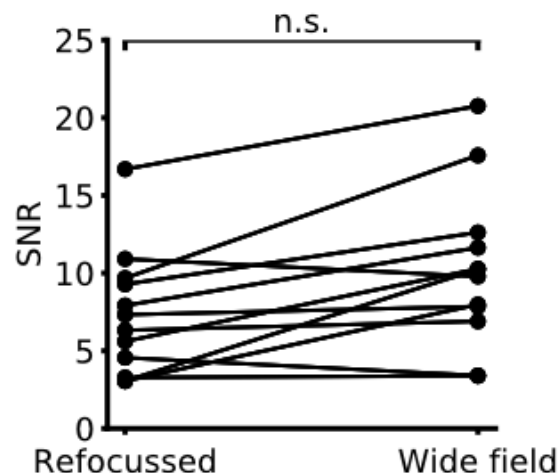341 intensifying with increasing iteration number.

20

Fig 5 Comparison of Light field and Wide Field SNR. Points correspond to mean SNR between paired light field and wide field trials. Light field microscopy SNR does not differ significantly from wide field. For 8/12 trials we included a correction factor due to a misalignment in the LFM as discussed in section 2.3.3.

342 *3.5 Temporal signal SNR is Unaffected by Light Field Imaging*

343 We measured the SNR for paired wide field and refocused light field imaging trials in the same

344 cells. For 8/12 trials we included a correction factor due to a misalignment in the LFM as discussed

345 in section 2.3.3. The SNR did not change significantly between the light field and wide field cases

346 (Wilcoxon signed rank test, n = 12 cells from 12 slices and 4 mice, $z = 32$, $p = 0.6$), with a median

347 light field SNR of 8.4 (5.2, 11.4) and a median wide field SNR of 10.0 (7.6, 11.9).

348 **4 Discussion**

349 We have shown that LFM enables 3D sub-cellular GEVI imaging of somatic and dendritic struc-

350 tures. We demonstrated that LFM enables simultaneous imaging of axially separated dendrites,

351 overcoming a key limitation of wide field imaging. We further showed that functional voltage

352 signals from dendrites could be axially resolved at different depths. This finding is key to demon-

353 strating LFM's utility for studies of dendritic integration or synaptic mapping.

354   We compared how synthetic refocussing and deconvolution-based reconstruction techniques

21

355 perform with respect to spatial signal localization and temporal SNR. Synthetic refocussing is

356 computationally simple and can be used to process light fields online, during an experiment, or

357 post hoc. Refocusing features better temporal signal SNR but poorer lateral and axial confinement

358 compared to deconvolution. Deconvolution has two major disadvantages: computational cost and

359 noise amplification. As the light field microscope PSF is not shift invariant it is described by a 5

360 dimensional matrix, complicating reconstruction. The periodicity it displays under lateral shifts by

361 integer multiples of the microlens pitch, however, enable deconvolution to be performed efficiently

362 by using FFT-based convolutions. Despite this, even small increases in lateral sampling in the de-

363 convolved volume increase the computational cost of reconstruction drastically. Reconstructing

364 n_z z-planes in a volume with a lateral increase in sampling over the native LFM sampling of m

365 requires $2 \times n_z \times m^2$ 2D convolutions per iteration, precluding online image processing. Sec-

366 ondly, both Richardson-Lucy and ISRA tend to amplify noise in their outputs due to their lack of

367 regularization.[78] This noise may be acceptable when imaging high-SNR calcium signals, however

368 it can dominate small, dim voltage signals. Incorporating regularization into the deconvolution

369 approaches to suppress noise overfitting could also ameliorate deconvolution's effects on temporal

370 SNR.

371   In this study we imaged VSFP-Butterfly 1.2, an older generation probe. GEVI technology

372 has advanced dramatically recently, greatly increasing their sensitivity, and with these new sensors

373 noise amplification due to deconvolution in the light field volume reconstruction may become less

374 significant. Although VSFP-Butterfly 1.2 exhibits lower sensitivity than several recently reported

375 probes,[20,79–83] we were able to express it sparsely and strongly to enable single-cell GEVI imag-

376 ing without somatic restriction, which would preclude study of sub-cellular signals.[65,66] The slow

377 kinetics of the probe used in this study also enabled resolution of action potentials at 100 frames/s

22

378 without severe aliasing. Although we could resolve single-sweep signals, signal averaging was re-

379 quired to resolve smaller dendritic signals with adequate SNR. With a more recent GEVI, dendritic

380 processes could likely be resolved in single sweeps.

381   Newer voltage sensors can not immediately be combined with LFM, however, as they require

382 much faster sampling rates, typically between 500 - $1000\,\mathrm{Hz}$. Megapixel cameras with $1\,\mathrm{kHz}$ full-

383 frame readout rates are therefore needed to fully exploit these newer voltage indicators. Current

384 sCMOS cameras such as the one used in this study can achieve these imaging rates by reducing the

385 FOV to a small central strip of the image sensor. This, however, is particularly detrimental to LFM

386 compared to wide field imaging as the LFM PSF spreads information about each point widely

387 across the image sensor for objects away from the focal plane. If only a small strip of the sensor

388 is imaged SNR will be greatly degraded as light is lost outside of this reduced FOV. We anticipate

389 that this issue will be steadily ameliorated as faster sCMOS sensor technology is developed.

390   A second issue arises with newer, faster GEVIs due to their requirement for much faster frame

391 rates. Deconvolving individual frames with these sensors would require a drastic increase in com-

392 putational resources and is likely untenable. Approaches have been developed for calcium imag-

393 ing light field time series which do not involve deconvolution of every frame.[61,84] In their current

394 form, however, these are unsuitable for reconstruction of subcellular light field voltage imaging

395 time series as they leverage the temporal and spatial characteristics of neuronal calcium imaging

396 as reconstruction priors. These priors, such as somatic signal localisation or sparse temporal activ-

397 ity, are not as applicable to subcellular voltage imaging signals, which are smaller, less temporally

398 sparse and arise from more morphologically intricate structures than neuronal somata.

399   Finally, in this study we compared the SNR between refocused LFM volumes and matched

400 wide field traces and found they did not differ significantly. This is expected, as apart from light

23

401 losses at the MLA, which are $< 15\%$ according to the manufacturer, there are no significant losses

402 of SNR to shot noise between wide field and light field microscopy. Together these results have the

403 potential to motivate further work and widespread application of light field microscopy to voltage

404 imaging owing to light fields high photon budget and ability to resolve neurons in three spatial

405 dimensions.

Disclosures

407 The authors declare that the research was conducted in the absence of any commercial or financial

408 relationships that could be construed as a potential conflict of interest.

Acknowledgements

Author Contributions

418 PQ, CLH, SRS and AJF conceived and designed the experiments. CLH and AJF designed the

419 light field optics. PQ and CLH performed experiments. PQ, CLH, AJF and SRS designed the

420 analysis. PQ, HVJ, PS, and PLD developed the deconvolution approach. CS and TK developed

421 and prepared animals with strong GEVI expression limited to a sparse neuronal subpopulation.

422 PQ and MN developed the light field PSF model. PQ analyzed the data and wrote the paper. All

423 authors contributed to manuscript revision and approved the final manuscript.

Data, Materials, and Code Availability

425 The datasets and code generated for this study are available on request to the corresponding author.

426 *References*

427 1 A. Foust, M. Popovic, D. Zecevic, *et al.*, "Action Potentials Initiate in the Axon Initial Seg-

428   ment and Propagate through Axon Collaterals Reliably in Cerebellar Purkinje Neurons," *The*

429   *Journal of Neuroscience* **30**(20), 6891–6902 (2010).

430 2 A. J. Foust, Y. Yu, M. Popovic, *et al.*, "Somatic membrane potential and kv1 channels control

431   spike repolarization in cortical axon collaterals and presynaptic boutons," *Journal of Neuro-*

432   *science* **31**(43), 15490–15498 (2011).

433 3 M. A. Popovic, X. Gao, N. T. Carnevale, *et al.*, "Cortical dendritic spine heads are not electri-

434   cally isolated by the spine neck from membrane potential signals in parent dendrites," *Cere-*

435   *bral Cortex* **24**, 385–395 (2014).

436 4 K. Holthoff, D. Zecevic, and A. Konnerth, "Rapid time course of action potentials in spines

437   and remote dendrites of mouse visual cortex neurons," *Journal of Physiology* **588**, 1085–1096

438   (2010).

439 5 L. M. Palmer and G. J. Stuart, "Membrane potential changes in dendritic spines during ac-

440   tion potentials and synaptic input.," *The Journal of neuroscience : the official journal of the*

441   *Society for Neuroscience* **29**(21), 6897–6903 (2009).

442 6 D. S. Peterka, H. Takahashi, and R. Yuste, "Imaging voltage in neurons," *Neuron* **69**(1), 9–21

443   (2011).

444 7 M. Djurisic, S. Antic, W. R. Chen, *et al.*, "Voltage imaging from dendrites of mitral cells:

445   Epsp attenuation and spike trigger zones," *Journal of Neuroscience* **24**(30), 6703–6714

446   (2004).

447 8 C. J. Roome and B. Kuhn, "Simultaneous dendritic voltage and calcium imaging and somatic

448   recording from purkinje neurons in awake mice," *Nature communications* **9**(1), 1–14 (2018).

449 9 M. Canepari, S. Willadt, D. Zecevic, *et al.*, "Imaging inhibitory synaptic potentials using

450   voltage sensitive dyes," *Biophysical journal* **98**(9), 2032–2040 (2010).

451 10 S. D. Antic, R. M. Empson, and T. Knöpfel, "Voltage imaging to understand connections and

452   functions of neuronal circuits," *Journal of neurophysiology* **116**(1), 135–152 (2016).

453 11 T. Kwon, M. Sakamoto, D. S. Peterka, *et al.*, "Attenuation of synaptic potentials in dendritic

454   spines," *Cell reports* **20**(5), 1100–1110 (2017).

455 12 S. Chamberland, H. H. Yang, M. M. Pan, *et al.*, "Fast two-photon imaging of subcellular

456   voltage dynamics in neuronal tissue with genetically encoded indicators," *Elife* **6**, e25690

457   (2017).

458 13 S. D. Antic, "Action potentials in basal and oblique dendrites of rat neocortical pyramidal

459   neurons," *The Journal of physiology* **550**(1), 35–50 (2003).

460 14 S. Antic, G. Major, and D. Zecevic, "Fast optical recordings of membrane potential changes

461   from dendrites of pyramidal neurons," *Journal of neurophysiology* **82**(3), 1615–1621 (1999).

462 15 F. Anselmi, C. Ventalon, A. Begue, *et al.*, "Three-dimensional imaging and photostimulation

26

463   by remote-focusing and holographic light patterning," *Proceedings of the National Academy*

464   *of Sciences* **108**(49), 19504–19509 (2011).

465 16 S. Quirin, N. Vladimirov, C.-T. Yang, *et al.*, "Calcium imaging of neural circuits with ex-

466   tended depth-of-field light-sheet microscopy," *Optics letters* **41**(5), 855–858 (2016).

467 17 R. Tomer, M. Lovett-Barron, I. Kauvar, *et al.*, "Sped light sheet microscopy: fast mapping of

468   biological system structure and function," *Cell* **163**(7), 1796–1806 (2015).

469 18 K. F. Ahrens, B. Heider, H. Lee, *et al.*, "Two-photon scanning microscopy of in vivo sensory

470   responses of cortical neurons genetically encoded with a fluorescent voltage sensor in rat,"

471   *Frontiers in neural circuits* **6**, 15 (2012).

472 19 W. Akemann, M. Sasaki, H. Mutoh, *et al.*, "Two-photon voltage imaging using a genetically

473   encoded voltage indicator," *Scientific reports* **3**, 2231 (2013).

474 20 V. Villette, M. Chavarha, I. K. Dimov, *et al.*, "Ultrafast two-photon imaging of a high-gain

475   voltage indicator in awake behaving mice," *Cell* **179**(7), 1590–1608 (2019).

476 21 J. Bewersdorf, R. Pick, and S. W. Hell, "Multifocal multiphoton microscopy," *Optics letters*

477   **23**(9), 655–657 (1998).

478 22 K. H. Kim, C. Buehler, K. Bahlmann, *et al.*, "Multifocal multiphoton microscopy based on

479   multianode photomultiplier tubes," *Optics express* **15**(18), 11658–11678 (2007).

480 23 T. Nielsen, M. Fricke, D. Hellweg, *et al.*, "High efficiency beam splitter for multifocal multi-

481   photon microscopy," *Journal of microscopy* **201**(3), 368–376 (2001).

482 24 Y. Shao, J. Qu, X. Peng, *et al.*, "Addressable multiregional and multifocal multiphoton mi-

483   croscopy based on a spatial light modulator," *Journal of biomedical optics* **17**(3), 030505

484   (2012).

485   25 P. Quicke, S. Reynolds, M. Neil, *et al.*, "High speed functional imaging with source localized

486   multifocal two-photon microscopy," *Biomedical Optics Express* **9**, 3678 (2018).

487   26 J. Wu, Y. Liang, S. Chen, *et al.*, "Kilohertz two-photon fluorescence microscopy imaging of

488   neural activity in vivo," *Nature Methods* **17**(3), 287–290 (2020).

489   27 T. Zhang, O. Hernandez, R. Chrapkiewicz, *et al.*, "Kilohertz two-photon brain imaging in

490   awake mice," *Nature methods* **16**(11), 1119–1122 (2019).

491   28 R. Prevedel, A. J. Verhoef, A. J. Pernía-Andrade, *et al.*, "Fast volumetric calcium imaging

492   across multiple cortical layers using sculpted light.," *Nature methods* **13**, 1021–1028 (2016).

493   29 S. Weisenburger, F. Tejera, J. Demas, *et al.*, "Volumetric ca2+ imaging in the mouse brain

494   using hybrid multiplexed sculpted light microscopy," *Cell* **177**(4), 1050–1066 (2019).

495   30 M. Žurauskas, S. Waddell, M. Frade-Rodriguez, *et al.*, "Rapid adaptive remote focusing

496   microscope for sensing of volumetric neural activity," *Biomedical Optics Express* **8**, 4369

497   (2017).

498   31 A. Kazemipour, O. Novak, D. Flickinger, *et al.*, "Kilohertz frame-rate two-photon tomogra-

499   phy," *Nature methods* **16**(8), 778 (2019).

500   32 H. Dana, A. Marom, S. Paluch, *et al.*, "Hybrid multiphoton volumetric functional imaging of

501   large-scale bioengineered neuronal networks," *Nature communications* **5**, 3997 (2014).

502   33 M. B. Ahrens, M. B. Orger, D. N. Robson, *et al.*, "Whole-brain functional imaging at cellular

503   resolution using light-sheet microscopy," *Nat Methods* **10**(5), 413–420 (2013).

504   34 J. Huisken, J. Swoger, F. Del Bene, *et al.*, "Optical sectioning deep inside live embryos by

505   selective plane illumination microscopy," *Science* **305**(5686), 1007–1009 (2004).

28

506 35 P. J. Keller and M. B. Ahrens, "Visualizing whole-brain activity and development at the
507   single-cell level using light-sheet microscopy," *Neuron* **85**(3), 462–483 (2015).

508 36 M. B. Bouchard, V. Voleti, C. S. Mendes, *et al.*, "Swept confocally-aligned planar excitation
509   (SCAPE) microscopy for high-speed volumetric imaging of behaving organisms," *Nature*
510   *Photonics* **9**, 113–119 (2015).

511 37 D. Oron, E. Tal, and Y. Silberberg, "Scanningless depth-resolved microscopy," *Optics express*
512   **13**(5), 1468–1476 (2005).

513 38 G. Zhu, J. Van Howe, M. Durst, *et al.*, "Simultaneous spatial and temporal focusing of fem-
514   tosecond pulses," *Optics express* **13**(6), 2153–2159 (2005).

515 39 T. Schrödel, R. Prevedel, K. Aumayr, *et al.*, "Brain-wide 3d imaging of neuronal activity in
516   caenorhabditis elegans with sculpted light," *Nature methods* **10**(10), 1013 (2013).

517 40 C. J. Rowlands, D. Park, O. T. Bruns, *et al.*, "Wide-field three-photon excitation in biological
518   samples," *Light: Science & Applications* **6**, e16255–e16255 (2017).

519 41 O. Therrien, B. Aubé, S. Pagès, *et al.*, "Wide-field multiphoton imaging of cellular dynamics
520   in thick tissue by temporal focusing and patterned illumination," *Biomedical optics express*
521   **2**(3), 696–704 (2011).

522 42 A. J. Foust, V. Zampini, D. Tanese, *et al.*, "Computer-generated holography enhances volt-
523   age dye fluorescence discrimination in adjacent neuronal structures," *Neurophotonics* **2**(2),
524   021007 (2015).

525 43 V. Nikolenko, B. O. Watson, R. Araya, *et al.*, "Slm microscopy: scanless two-photon imaging
526   and photostimulation using spatial light modulators," *Frontiers in neural circuits* **2**, 5 (2008).

29

527 44 S. Bovetti, C. Moretti, S. Zucca, *et al.*, "Simultaneous high-speed imaging and optogenetic

528   inhibition in the intact mouse brain," *Scientific reports* **7**, 40041 (2017).

529 45 D. Tanese, J.-Y. Weng, V. Zampini, *et al.*, "Imaging membrane potential changes from den-

530   dritic spines using computer-generated holography," *Neurophotonics* **4**(3), 031211 (2017).

531 46 E. J. Botcherby, R. Juškaitis, and T. Wilson, "Scanning two photon fluorescence microscopy

532   with extended depth of field," *Optics Communications* **268**, 253–260 (2006).

533 47 R. Lu, W. Sun, Y. Liang, *et al.*, "Video-rate volumetric functional imaging of the brain at

534   synaptic resolution," *Nature Neuroscience* **20**, 620–628 (2017).

535 48 A. Song, A. S. Charles, S. A. Koay, *et al.*, "Volumetric two-photon imaging of neurons using

536   stereoscopy (vtwins)," *Nature methods* **14**(4), 420–426 (2017).

537 49 M. Levoy, R. Ng, A. Adams, *et al.*, "Light field microscopy," in *ACM SIGGRAPH 2006*

538   *Papers on - SIGGRAPH '06*, **25**(3), 924, ACM Press, (New York, New York, USA) (2006).

539 50 M. Broxton, L. Grosenick, S. Yang, *et al.*, "Wave optics theory and 3-D deconvolution for

540   the light field microscope," *Optics Express* **21**(21), 25418 (2013).

541 51 W. H. Richardson, "Bayesian-Based Iterative Method of Image Restoration*," *Journal of the*

542   *Optical Society of America* **62**, 55 (1972).

543 52 L. B. Lucy, "An iterative technique for the rectification of observed distributions," *The Astro-*

544   *nomical Journal* **79**, 745 (1974).

545 53 M. E. Daube-Witherspoon and G. Muehllehner, "An Iterative Image Space Reconstruction

546   Algorithm Suitable for Volume ECT," *IEEE Transactions on Medical Imaging* **5**, 61–66

547   (1986).

548 54 H. Li, C. Guo, D. Kim-Holzapfel, *et al.*, "Fast, volumetric live-cell imaging using high-
549   resolution light-field microscopy," *Biomedical Optics Express* **10**, 29 (2019).

550 55 C. Guo, W. Liu, X. Hua, *et al.*, "Fourier light-field microscopy," *Opt. Express* **27**, 25573–
551   25594 (2019).

552 56 X. Lin, J. Wu, G. Zheng, *et al.*, "Camera array based light field microscopy," *Biomedical*
553   *optics express* **6**(9), 3179–3189 (2015).

554 57 N. Cohen, S. Yang, A. Andalman, *et al.*, "Enhancing the performance of the light field mi-
555   croscope using wavefront coding," *Optics express* **22**(20), 24817–24839 (2014).

556 58 R. Prevedel, Y.-G. Yoon, M. Hoffmann, *et al.*, "Simultaneous whole-animal 3D imaging of
557   neuronal activity using light-field microscopy.," *Nature methods* **11**(7), 727–30 (2014).

558 59 N. Wagner, N. Norlin, J. Gierten, *et al.*, "Instantaneous isotropic volumetric imaging of fast
559   biological processes," *Nature methods* **16**(6), 497–500 (2019).

560 60 L. M. Grosenick, M. Broxton, C. K. Kim, *et al.*, "Identification Of Cellular-Activity Dynam-
561   ics Across Large Tissue Volumes In The Mammalian Brain," *bioRxiv* , 132688 (2017).

562 61 T. Nöbauer, O. Skocek, A. J. Pernía-Andrade, *et al.*, "Video rate volumetric Ca2+ imaging
563   across cortex using seeded iterative demixing (SID) microscopy," *Nature Methods* **14**, 811–
564   818 (2017).

565 62 O. Skocek, T. Nöbauer, L. Weilguny, *et al.*, "High-speed volumetric imaging of neuronal
566   activity in freely moving rodents," *Nature Methods* **15**, 429–432 (2018).

567 63 S. Aimon, T. Katsuki, T. Jia, *et al.*, "Fast near-whole–brain imaging in adult drosophila during
568   responses to stimuli and behavior," *PLoS biology* **17**(2), e2006732 (2019).

569   64 L. Cong, Z. Wang, Y. Chai, *et al.*, "Rapid whole brain imaging of neural activity in freely
570   behaving larval zebrafish (Danio rerio)," *eLife* **6** (2017).

571   65 P. Quicke, C. Song, E. J. McKimm, *et al.*, "Single-neuron level one-photon voltage imaging
572   with sparsely targeted genetically encoded voltage indicators.," *Frontiers in Cellular Neuro-*
573   *science* **13**, 39 (2019).

574   66 C. Song, Q. Do, S. Antic, *et al.*, "Transgenic Strategies for Sparse but Strong Expression of
575   Genetically Encoded Voltage and Calcium Indicators," *International Journal of Molecular*
576   *Sciences* **18**, 1461 (2017).

577   67 P. Quicke, C. L. Howe, P. Song, *et al.*, "Calculation of high numerical aperture lightfield
578   microscope point spread functions," in *Imaging and Applied Optics 2019 (COSI, IS, MATH,*
579   *pcAOP)*, CW4A.2, OSA, (Washington, D.C.) (2019).

580   68 P. Quicke, *Improved methods for functional neuronal imaging with genetically encoded volt-*
581   *age indicators*. PhD thesis, Imperial College London (2019).

582   69 W. Akemann, H. Mutoh, A. Perron, *et al.*, "Imaging neural circuit dynamics with a voltage-
583   sensitive fluorescent protein.," *Journal of neurophysiology* **108**, 2323–37 (2012).

584   70 M. Mayford, M. E. Bach, Y. Y. Huang, *et al.*, "Control of memory formation through regu-
585   lated expression of a CaMKII transgene.," *Science (New York, N.Y.)* **274**(5293), 1678–1683
586   (1996).

587   71 J. A. Harris, K. E. Hirokawa, S. A. Sorensen, *et al.*, "Anatomical characterization of Cre
588   driver mice for neural circuit mapping and manipulation," *Frontiers in Neural Circuits* **8**, 76
589   (2014).

590   72 L. Madisen, A. R. Garner, D. Shimaoka, *et al.*, "Transgenic Mice for Intersectional Targeting

32

591   of Neural Sensors and Effectors with High Specificity and Performance," *Neuron* **85**, 942–

592   958 (2015).

593   73 J. T. Ting, T. L. Daigle, Q. Chen, *et al.*, "Acute brain slice methods for adult and aging ani-

594   mals: application of targeted patch clamp analysis and optogenetics.," *Methods in molecular*

595   *biology (Clifton, N.J.)* **1183**, 221–42 (2014).

596   74 A. D. Edelstein, M. A. Tsuchida, N. Amodaj, *et al.*, "Advanced methods of microscope

597   control using μManager software.," *Journal of biological methods* **1**(2), 10 (2014).

598   75 P. Virtanen, R. Gommers, T. E. Oliphant, *et al.*, "SciPy 1.0: Fundamental Algorithms for

599   Scientific Computing in Python," *Nature Methods* **17**, 261–272 (2020).

600   76 R. Ng, M. Levoy, M. Brédif, *et al.*, "Light Field Photography with a Hand-Held Plenoptic

601   Camera – Stanford Tech Report CTSR 2005-02," tech. rep. (2005).

602   77 E. Thiébaut, "Introduction to image reconstruction and inverse problems," in *NATO Science*

603   *Series II., Mathematics, Physics and Chemistry*, R. Foy and F.-C. Foy, Eds., 397, Springer

604   (2005).

605   78 N. Dey, L. Blanc-feraud, C. Zimmer, *et al.*, "Richardson-Lucy Algorithm with Total Vari-

606   ation Regularization for 3D Confocal Microscope Deconvolution," *Microscopy Research &*

607   *Technique* **69**(4), 260–266 (2006).

608   79 A. S. Abdelfattah, T. Kawashima, A. Singh, *et al.*, "Bright and photostable chemigenetic

609   indicators for extended in vivo voltage imaging," *Science* **365**(6454), 699–704 (2019).

610   80 Y. Adam, J. J. Kim, S. Lou, *et al.*, "Voltage imaging and optogenetics reveal behaviour-

611   dependent changes in hippocampal dynamics," *Nature* **569**(7756), 413–417 (2019).

612 81 K. D. Piatkevich, E. E. Jung, C. Straub, *et al.*, "A robotic multidimensional directed evolution

613   approach applied to fluorescent voltage reporters," *Nature Chemical Biology* **14**, 352–360

614   (2018).

615 82 B. Yi, B. E. Kang, S. Lee, *et al.*, "A dimeric fluorescent protein yields a bright, red-shifted

616   GEVI capable of population signals in brain slice," *Scientific Reports* **8**(1), 15199 (2018).

617 83 M. Kannan, G. Vasan, C. Huang, *et al.*, "Fast, in vivo voltage imaging using a red fluorescent

618   indicator," *Nature methods* **15**(12), 1108–1116 (2018).

619 84 N. C. Pégard, H.-Y. Liu, N. Antipa, *et al.*, "Compressive light-field microscopy for 3d neural

620   activity recording," *Optica* **3**(5), 517–524 (2016).